Available online at www.sciencedirect.com
ScienceDirect
Trans. Nonferrous Met. Soc. China 35(2025) 13−29
Transactions of Nonferrous Metals Society of China
www.tnmsc.cn

Mechanism of cryorolling and aging treatment for enhancing corrosion properties of 2195 Al−Li alloy

Yue XIAO[1,2], Wen-shuai WANG[1,2], Waqas FARID[1,2], Li-hua ZHANG[1,2], Charlie KONG[3], Hai-liang YU[1,2]

1. State Key Laboratory of Precision Manufacturing for Extreme Service Performance, Central South University, Changsha 410083, China;
2. Light Alloy Research Institute, Central South University, Changsha 410083, China;
3. Mark Wainwright Analytical Centre, University of New South Wales, Sydney, NSW 2052, Australia

Received 11 May 2023; accepted 21 December 2023

Abstract: The impact of cryorolling (CR) and room temperature rolling (RTR) followed by artificial aging on the corrosion characteristics of 2195 Al−Li alloy (AA2195) was studied. Transmission electron microscope, scanning electron microscope, optical microscope, intergranular corrosion experiment, and electrochemical experiment were used. Throughout different stages of aging treatment, the corrosion behavior of both CR and RTR samples exhibited a sequential progression of pitting corrosion, followed by intergranular corrosion, and then pitting corrosion again. The corrosion rates of both samples initially showed an increase, followed by a gradual stabilization over time. The size and density of T_1 phase significantly influenced the corrosion performance of the alloy. During the peak aging and over-aging stages, the CR sample exhibited superior corrosion resistance to the RTR sample, attributed to its finer T_1 phase.

Key words: 2195 Al−Li alloy; cryorolling; aging treatment; corrosion performance

1 Introduction

Al−Li alloys show considerable application prospects in the aviation and aerospace industries due to their advantages, such as low density, high specific strength, and high elastic modulus [1−2]. These alloys find extensive application in various components of aviation aircraft, including deep-cooling fuel tanks, underwing stringers, fuselage skin, horizontal stabilizers, upper and lower wings, fuselage pressure chambers, and internal structures, highlighting their versatile utility in these sectors. The components like horizontal stabilizers, aircraft upper wings, and fuselage pressure chambers demand materials with stringent mechanical and corrosion properties [3]. The process of rolling deformation combined with aging treatment plays an important role in improving the mechanical properties of the alloy. However, previous studies indicate that aging treatment gradually deteriorates the corrosion properties of Al−Li alloy [4]. Therefore, it is imperative to identify a method that not only enhances the mechanical properties of the alloy but also ensures the preservation of corrosion resistance to the greatest extent possible.

Furthermore, the primary methods for enhancing the mechanical properties of Al alloy involve increasing the dislocation density and reducing the grain size of alloy [5]. It is widely acknowledged that ultra-fine-grained metals exhibit exceptional characteristics, including ultra-high

Corresponding author: Hai-liang YU, Tel/Fax: +86-18511635397, E-mail: yuhailiang@csu.edu.cn;
Li-hua ZHANG, email: zhanglihua_csu@163.com
https://doi.org/10.1016/S1003-6326(24)66662-8

strength and plasticity, as well as superior fatigue and corrosion resistance [6,7]. Previous studies show that cryorolling (CR) stands out as an effective method for preparing ultrafine-grained materials. Along these lines, LI et al [8] successfully fabricated an Al−3.6Cu−1Li alloy, demonstrating both high strength and toughness through the implementation of cryorolling and aging treatment. In a study by WU et al [9], the effect of asymmetric cryorolling on a medium-entropy CrCoNi alloy was investigated. After annealing, the asymmetric-cryorolled samples displayed superior strength and ductility compared to those subjected to asymmetric rolling. Additionally, LI et al [10] fabricated pure nickel sheets that combined high strength with good ductility through the utilization of cryorolling and low-temperature short-time annealing. Cryogenic temperatures during CR play a crucial role in enhancing dislocation density, consequently leading to an improvement in the mechanical properties of materials. Subsequent heat treatment further amplifies the strength and plasticity of materials [11−14]. The enhanced mechanical properties of alloys after CR are attributed to the combined effects of precipitation strengthening, grain boundary strengthening, and dislocation strengthening. As the aging treatment progresses, precipitation strengthening gradually emerges as the predominant strengthening mechanism [12]. Thus, it is evident that CR significantly influences the precipitated phase of the alloy.

The corrosion resistance of Al−Li alloy is notably influenced by factors such as the type, distribution, and density of the precipitated phase [15−19]. Previous studies highlighted that micro-electric couple formed due to the potential difference between the precipitated phase and the Al matrix is the key factor promoting the corrosion behavior of Al alloy [20−22]. In Al−Li alloy, with the addition of Li and Cu, the main precipitated phases include the T_1 phase (Al_2CuLi), δ' phase (Al_3Li), and θ' phase (Al_2Cu) [23−26]. The corrosion characteristics of these precipitated phases in a 0.6 mol/L NaCl solution have been thoroughly studied and discussed. The δ' and θ' phases, owing to their active Li content, exhibit a more negative corrosion potential, functioning as anodes in the electric coupling process. In contrast, the T_1 phase plays a more intricate role in the corrosion process. Initially, owing to the presence of Li, the T_1 phase selectively dissolves as the anode. As both Li and Al disappear, the remaining Cu-rich phase transforms into the cathode, perpetuating the anodic dissolution of the Al matrix [27−31]. Earlier investigations have shown that the T_1 phase exerts the most significant influence on the corrosion performance of Al−Li alloy. With an increase in aging time, the massive precipitation of the T_1 phase is associated with a decline in the corrosion performance of Al−Li alloy.

The precipitation in the Al−Li alloys prepared using CR differs from that in room-temperature rolled sheets, thereby affecting both the mechanical and corrosion properties of the alloys. Despite this, limited research exists on the corrosion properties of Al−Li alloy prepared via CR. To address these aforementioned issues, our study aims to explore the impact of CR on the corrosion characteristics of Al−Li alloy, shedding light on its underlying mechanisms. This research holds significant value in attaining Al−Li alloys with exceptional corrosion resistance and comprehensive mechanical properties, ultimately fostering advancements in the aviation industry.

2 Experimental

The AA2195 alloy utilized was supplied by the China Space Technology Research Institute, with an initial thickness of 2 mm. The chemical composition of the alloy was obtained using inductively coupled plasma atomic emission spectroscopy (ICP-AES, Spectro Blue Sop), with the results listed in Table 1.

Table 1 Chemical composition of as-received Al−Li plate (wt.%)

Cu	Li	Mg	Ag	Zr	Fe	Si	Ti	Al
3.75	1.07	0.52	0.39	0.12	0.059	0.047	0.041	Bal.

Figure 1(a) depicts the material preparation process and method used, while Fig. 1(b) shows the orientation diagram highlighting the rolling direction (RD), transverse direction (TD), and normal direction (ND). The plates underwent solid solution treatment at 500 °C for 0.5 h and quenching in cold water, followed by CR and room-temperature rolling (RTR). During CR, the AA2195 alloy was first immersed in a liquid N_2 container for

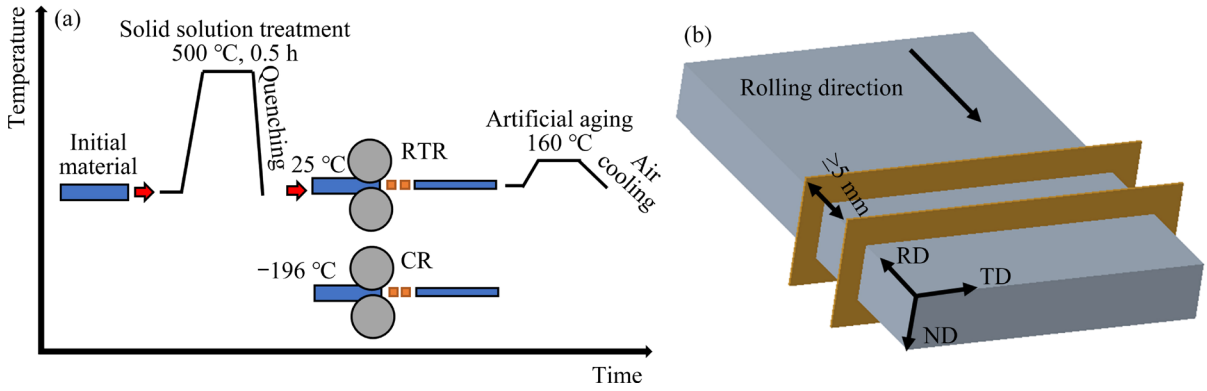

Fig. 1 Schematic diagram of AA2195 plate with different rolling and aging treatments (a), and schematic diagram of corrosion test sample (b)

30 min to stabilize its temperature at −196 °C, after which multiple passes of CR were performed. The alloy was then re-immersed in the liquid N_2 container for 5 min before each pass of CR. Notably, the rolling reduction remained consistent in each pass for both RTR and CR, not exceeding 5% of the thickness of the initial alloy until the total rolling reduction reached 50%.

Following the rolling process, the alloy was subjected to aging at 160 °C for varying durations. The CR and RTR samples with the aging time of 3, 12, 20, 80, 104, and 152 h were designated as CR 3 h, CR 12h, CR 20 h, CR 80 h, CR 104 h, CR 152 h, RTR 3 h, RTR 12 h, RTR 20 h, RTR 80 h, RTR 104 h, and RTR 152 h. The aging stage of the alloy was assessed through hardness testing conducted on a VTt-1000 Vickers hardness tester, by applying a load of 300 g with a load retention time of 15 s. The evolution of specific aging stages is shown in Fig. 2. The experimental results indicated that the CR sample reached its peak aging stage at 12 h, displaying a hardness of HV 188.45, whereas the RTR sample achieved the peak aging stage at 20 h, with its hardness of HV 187.00.

Furthermore, the RD−TD surface of the alloy underwent a successive grinding process with 800, 1000, 1200, and 1500 WC abrasives. After grinding, the sample was polished with 1.5 μm vajra plaster. Subsequently, sample surface was thoroughly rinsed with alcohol and then air-dried. The corrosion morphology and electrochemical properties of the samples were studied through intergranular corrosion (IGC) tests, potentio-dynamic polarization, and electrochemical impedance spectroscopy (EIS) tests.

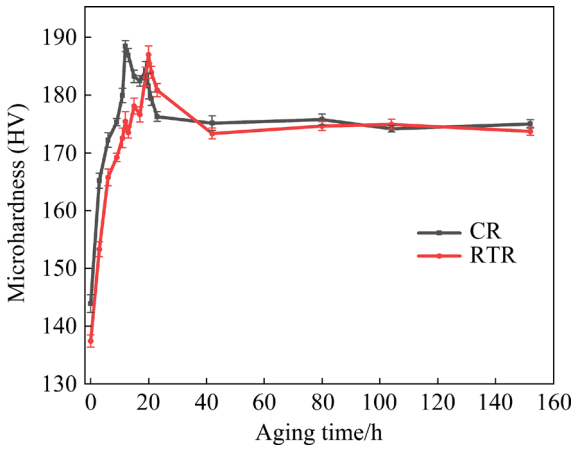

Fig. 2 Hardness evolution of alloy during artificial aging at 160 °C

IGC tests were conducted in strict accordance with GB T 7998 — 2005, with the non-polished surface being protected by epoxy resin. These tests took place in a constant temperature bath maintained at (35±2) °C, with an exposed surface area of 10 cm^2. Prior to soaking, the samples required pretreatment. The polished samples were initially treated with an alkali wash using a 10 wt.% NaOH solution, followed by rinsing with distilled water. Thereafter, the samples underwent pickling in a 30 wt.% HNO_3 solution until their surfaces were thoroughly cleaned, followed by rinsing with distilled water. The pretreated samples were immersed in a mixture of 57 g/L NaCl and 1 vol.% H_2O_2 for 6 h, maintaining a temperature of (35±2) °C using a constant-temperature water bath. Finally, the immersed samples were divided into three sections along the TD−ND direction to ensure that the cross sections of each sample were more than 5 mm apart, as depicted in Fig. 1(b).

Subsequently, the TD−ND surface of each sample was lapped and polished, and the optical microscope was employed to observe the evolution of corrosion patterns, including their maximum and average corrosion depths.

Further, potentiodynamic polarization and EIS tests were performed in a 3.5 wt.% NaCl solution using the Adminal electrochemical workstation (Squidstat Plus, USA). The experiments employed a conventional three-electrode cell with the saturated calomel electrode (SCE) as the reference electrode, a platinum plate as the counter electrode, and the test sample as the working electrode. Before conducting the potentiodynamic polarization and EIS tests, the sample was immersed in a 3.5 wt.% NaCl solution for 15 min to ensure the stabilization of its open circuit potential (OCP). The scanning rate during the potentiodynamic polarization test was 2 mV/s, and the exposed RD−TD surface was 1 cm^2. To prevent the oxidation, the samples were immediately washed with distilled water after the dynamic polarization test, and any water stain on surface were wiped with filter paper. Meanwhile, during EIS test, the perturbation was set at 5 mV, and the frequency range was from 100 kHz to 100 MHz. The obtained results were subjected to equivalent circuit fitting using Zahner Analysis software. Subsequently, the corrosion morphology of the RD−TD surface was observed using scanning electron microscopy (SEM, TM4000plus 15 kV).

The grain structure of CR and RTR samples at different aging stages was examined using an optical microscope. After polishing the TD−ND surface, the sample was etched with Barker reagent (1 mL HBF_4 and 49 mL distilled water) under the conditions of a voltage set to be 25 V, a current density of 0.05 A/cm^2, and a power-on time of 120 s. The microstructure of the aged samples was further characterized through transmission electron microscopy (TEM, FEI Tecnai G^2 20) at an acceleration voltage of 200 kV. The samples were reduced to a thickness of 100 μm via mechanical grinding and then shaped into disks with a diameter of 3.0 mm. These disks underwent dual-jet electrolytic polishing in a mixed solution comprising 30 vol.% HNO_3 and 70 vol.% methanol. The power supply voltage of the device was maintained at 25 V DC, and the solution temperature was roughly −20 °C. Each electrolytic polishing session lasted for 10−40 s.

3 Results and discussion

3.1 IGC analysis

Figures 3 and 4 display corrosion morphologies of samples immersed in a 57 g/L NaCl solution and a 1 vol.% H_2O_2 solution (maintained at (35±2) °C) for 6 h. Specifically, Figs. 3(a−f) and 4(a−f) illustrate that the corrosion trend changed along the TD−ND surface of samples aged for different time at 160 °C after CR and RTR, respectively. Corresponding maximum corrosion and average corrosion depth are presented in Fig. 5. As shown in Figs. 3(a, b), during aging at 160 °C for 3 h, the corrosion morphology of CR samples was primarily dominated by pitting, resulting in maximum and average corrosion depths of 75 and 62 μm, respectively. With an increase in aging time to 12 h, the corrosion morphology of CR samples changed from pitting corrosion to IGC, leading to maximum and average corrosion depths of 96 and 73 μm, respectively. As evident in Figs. 3(c, d), the IGC trend of CR samples became more pronounced with the prolonged aging time. The maximum corrosion depths were recorded at 103 and 135 μm after 20 and 80 h of aging, with average corrosion depths of 82 and 89 μm, respectively. In Figs. 3(e, f), upon reaching an aging time of 104 h, the corrosion mode of the CR samples began to shift toward pitting corrosion, although slight IGC occurred, resulting in the maximum and average corrosion depths of 134 and 81 μm, respectively. As the aging time was further extended to 152 h, the corrosion mode of CR samples changed primarily to pitting, with virtually no observable IGC.

As displayed in Figs. 4(a, b), when subjected to aging at 160 °C for 3 h, the corrosion morphology of the RTR samples featured pitting, with maximum and average corrosion depths measuring 73 and 56 μm, respectively. Upon reaching an aging time of 12 h, the RTR samples, unlike the CR samples, continued to exhibit predominately pitting corrosion alongside minor occurrences of IGC. The maximum and average corrosion depths were found to be 98 and 77 μm, respectively. As shown in Figs. 4(c, d), after 20 h of aging time, the corrosion morphology of RTR samples displayed typical IGC, featuring maximum and average corrosion depths of 119 and 98 μm, respectively. With further extension of the aging

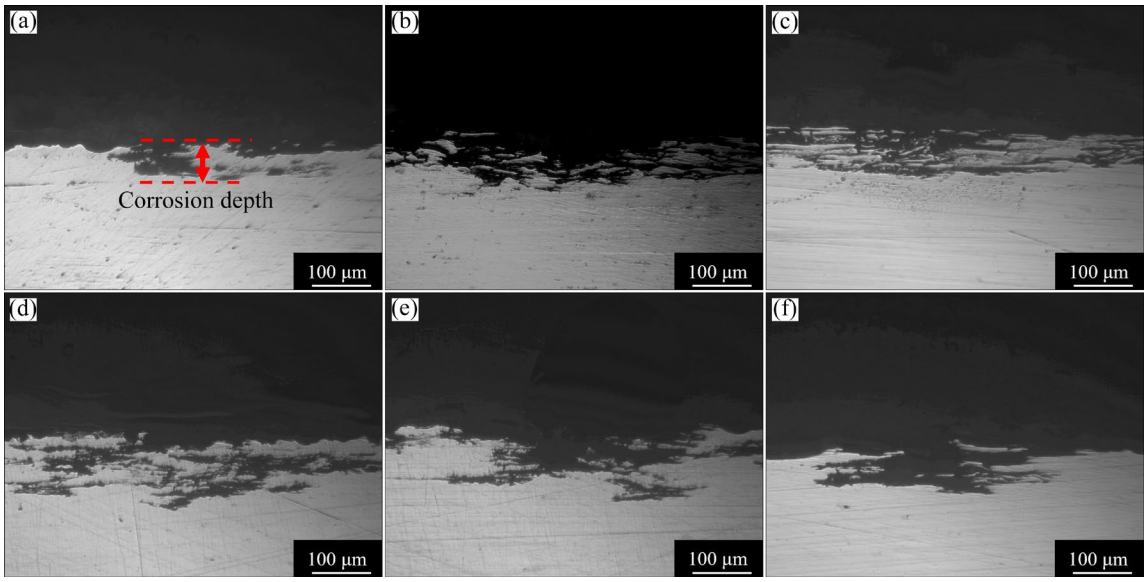

Fig. 3 Typical cross-section (TD−ND) corrosion profiles of CR samples after being soaked in 57 g/L NaCl and 1 vol.% H_2O_2 solution at (35±2) °C for 6 h and aging at 160 °C for 3 h (a), 12 h (b), 20 h (c), 80 h (d), 104 h (e) and 152 h (f)

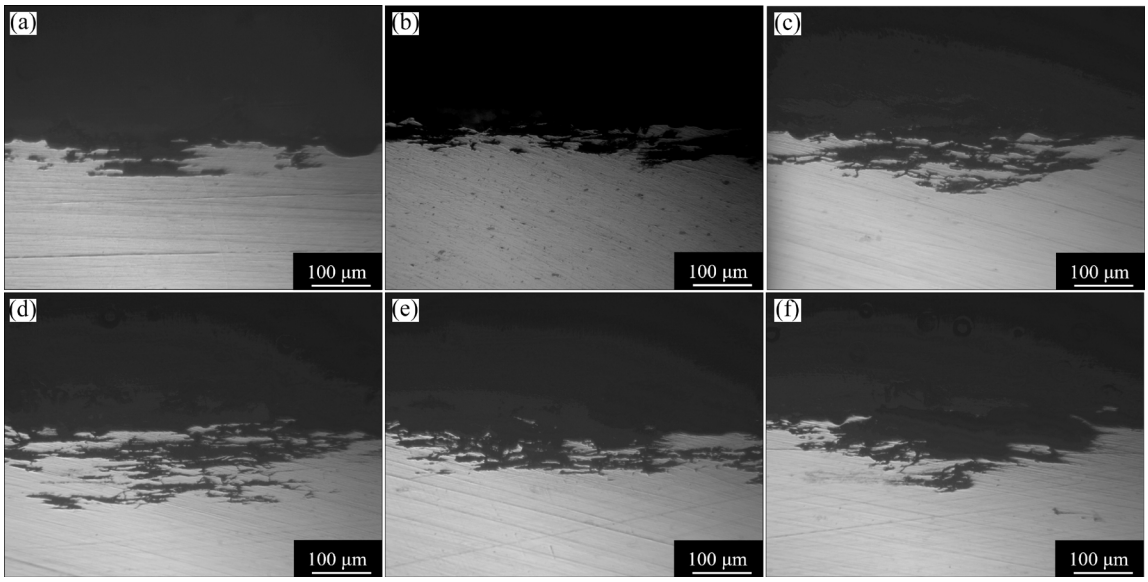

Fig. 4 Typical cross-section (TD−ND) corrosion profiles of RTR samples after being soaked in 57 g/L NaCl and 1 vol.% H_2O_2 solution at (35±2) °C for 6 h and aging at 160 °C for 3 h (a), 12 h (b), 20 h (c), 80 h (d), 104 h (e) and 152 h (f)

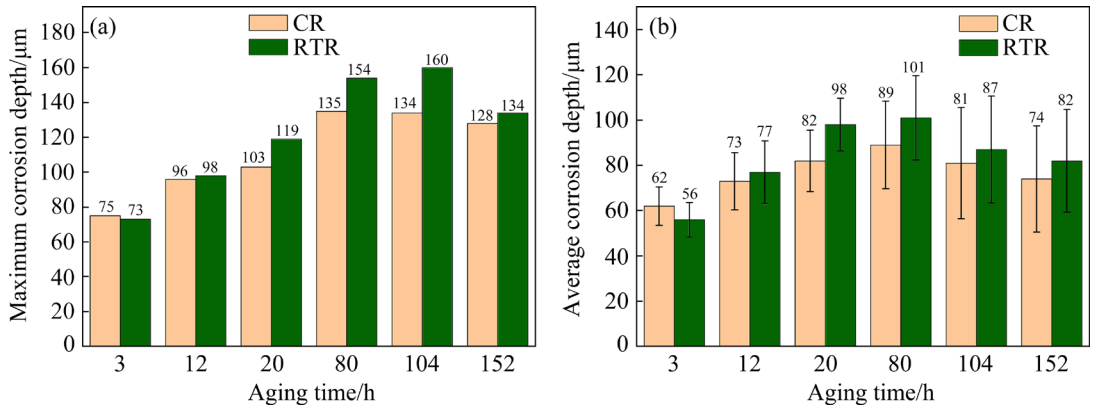

Fig. 5 Maximum corrosion depth (a) and average corrosion depth (b) on TD−ND surface of sample exposed to 57 g/L NaCl and 1 vol.% H_2O_2 solution at (35±2) °C for 6 h

time to 80 h, the samples still exhibited susceptibility to IGC; however, the corrosion areas were characterized by a discontinuous distribution. The corresponding maximum corrosion and average corrosion depth were recorded as 154 and 101 μm, respectively. Then, when the aging time was extended to 104 h, the RTR samples continued to demonstrate sensitivity to IGC, while the CR samples mainly showed sensitivity to intragranular corrosion, with a maximum corrosion depth of 160 μm and an average corrosion depth of 87 μm, as shown in Figs. 4(e, f). Finally, upon reaching an aging time of 152 h, the corrosion morphology of the samples shifted predominantly to pitting, with slight evidence of IGC. The maximum corrosion depth measured was 134 μm, with an average corrosion depth of 82 μm.

Therefore, the corrosion tendencies of both CR and RTR samples were similar, changing from pitting corrosion to IGC and ultimately back to pitting corrosion. The difference lies in the time of these transformations. For CR samples, the corrosion morphology was dominated by IGC at 12 h of aging, changing back to pitting corrosion at 104 h. In contrast, RTR samples exhibited typical IGC at 20 h, and pitting corrosion became the predominant corrosion mode at 152 h. After the occurrence of IGC, the metal surface retained a metallic luster. However, during this phase, IGC undermined the bond strength between grains, leading to a significant decline in the mechanical strength of the metal. Consequently, the mechanical properties of material experienced progressive deterioration [32−34]. Therefore, IGC was deemed more harmful than pitting corrosion. In conclusion, the CR samples aged at 160 °C traversed the potentially more detrimental IGC stage at a faster rate.

3.2 Potentiodynamic polarization analysis

Generally, in accordance with thermodynamic principles, more negative corrosion potential (φ_{corr}) of an alloy aligns with a greater susceptibility to electron loss, thereby promoting corrosion [35,36]. Therefore, a more negative corrosion potential represents higher electrochemical activity and poorer corrosion resistance of the alloy. The corrosion current density (J_{corr}) serves as a parameter to characterize the corrosion rate of the alloy, where a higher corrosion current density corresponds to a faster corrosion rate [37].

Figure 6 illustrates the potentiodynamic polarization curve of the alloy subjected to various aging time in a 3.5 wt.% NaCl solution. The corrosion parameters for both CR and RTR samples are summarized in Table 2. As shown in Fig. 6(a), at 3 h of aging time, the corrosion potential of the CR sample measured −673 mV vs SCE, while within the aging time range of 12−20 h, the corrosion potential of the alloy reduced from −700 mV to −709 mV vs SCE. With the aging time extending to 80 h, the corrosion potential of CR sample decreased to −728 mV vs SCE. Further extension of the aging time led only to a marginal reduction in the corrosion potential of CR samples, which remained in a stable state. The corrosion potential of CR samples at 104 and 152 h were observed to be −730 mV and –731 mV vs SCE, respectively.

Besides, the polarization curve of the RTR sample is shown in Fig. 6(b). At an aging time of 3 h, the corrosion potential of the sample measured −655 mV vs SCE. However, for aging time ranging from 12 to 80 h, the corrosion potential of the alloy

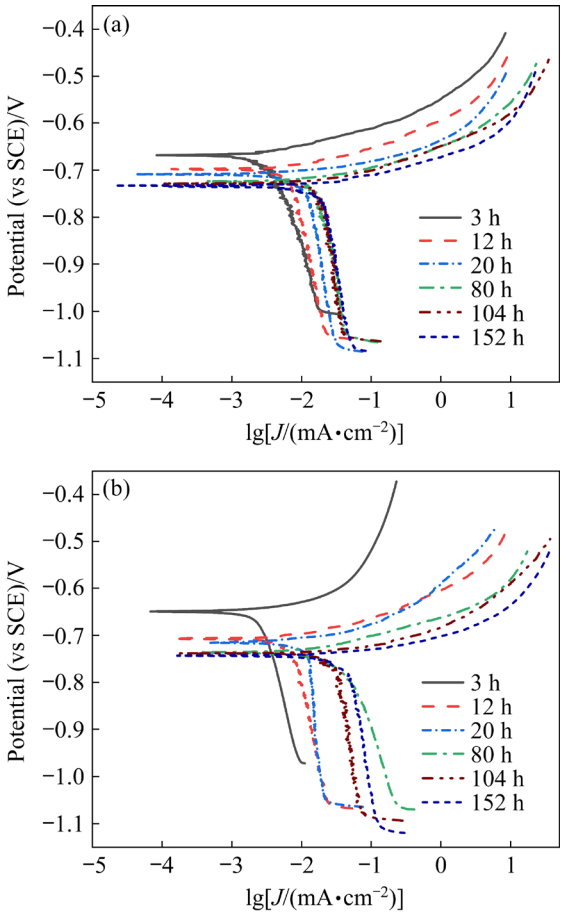

Fig. 6 Potentiodynamic polarization curves of samples in 3.5 wt.% NaCl solution: (a) CR; (b) RTR

Table 2 Corrosion parameters of alloys in 3.5% NaCl solution

Sample	φ_{corr}(vs SCE)/mV	J_{corr}/(μA·cm^{-2})
CR 3 h	−673	2.14
CR 12 h	−700	5.75
CR 20 h	−709	6.71
CR 80 h	−728	10.16
CR 104 h	−730	10.23
CR 152 h	−731	10.30
RTR 3 h	−655	1.44
RTR 12 h	−712	5.81
RTR 20 h	−718	10.54
RTR 80 h	−740	16.33
RTR 104 h	−740	16.44
RTR 152 h	−742	16.52

continuously declined, from −712 mV to −718 mV vs SCE, which further reduced to −740 mV vs SCE. In the aging time between 104 and 152 h, the corrosion potential of RTR samples reduced slightly compared to that at 80 h, measuring −740 mV and −742 mV vs SCE, respectively.

Additionally, the variation trend of polarization curves for both CR and RTR samples was similar, indicating a continuous decline in corrosion potential and a corresponding increase in corrosion current, followed by their gradual stabilization. However, the distinction laid in the differences in corrosion potential and corrosion current between the two samples at the same aging time. During the initial stages of aging, particularly at 3 h, the corrosion potential of the CR sample demonstrated a more negative value, coupled with a larger corrosion current compared to that of the RTR sample. Hence, the corrosion performance of the RTR sample surpassed that of the CR sample in the early aging period. Nonetheless, with the extension of the aging time from 12 to 152 h, the corrosion potential of the RTR sample became more negative, and the corrosion current was larger compared to the CR sample at the same aging time. This trend remained consistent across various stages, including both the transitional and stable phases of corrosion potential and corrosion current. In essence, the corrosion performance of CR sample outperformed the RTR sample starting from the 12 h aging. To validate this result and gain a deeper insight into the corrosion performance of the alloy, we examined the corrosion morphology of the RD−TD surface of both CR and RTR samples after the potentiodynamic polarization experiment using SEM. The relevant results are displayed in Figs. 7 and 8. In addition, the corrosion morphology of the TD−ND surface of CR and RTR samples was observed using OM after the potentiodynamic polarization experiment, and the results are presented in Figs. 9 and 10.

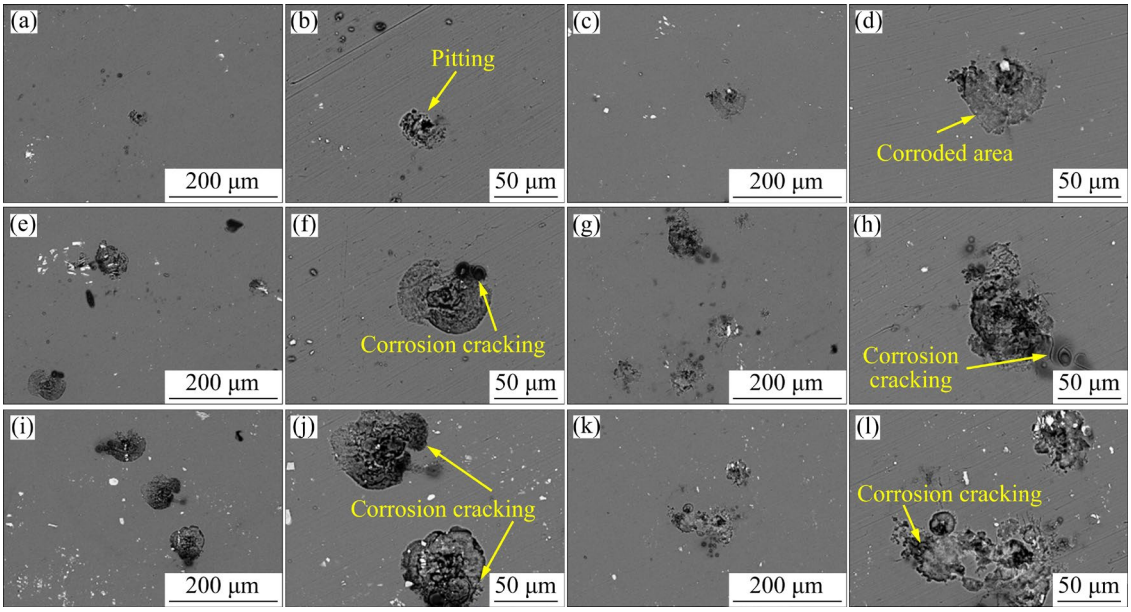

Fig. 7 Electrochemical corrosion morphologies on RD−TD surface of CR sample aged for different time after potentiodynamic polarization experiment: (a, b) 3 h; (c, d) 12 h; (e, f) 20 h; (g, h) 80 h; (i, j) 104 h; (k, l) 152 h

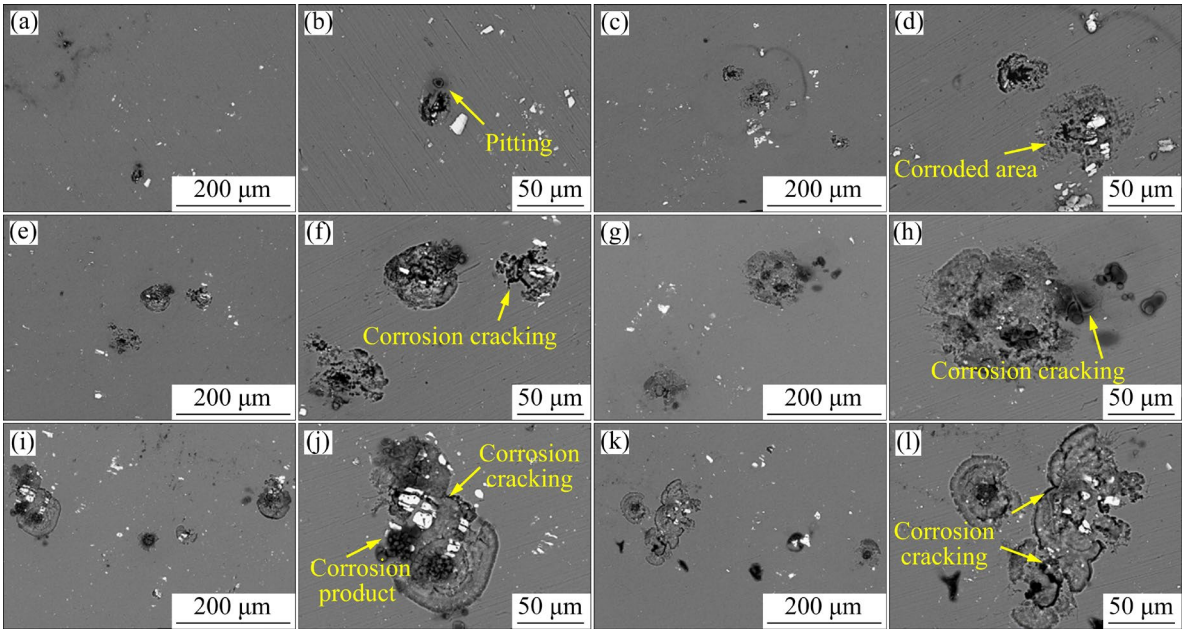

Fig. 8 Electrochemical corrosion morphologies on RD−TD surface of RTR sample aged for different time after potentiodynamic polarization experiment: (a, b) 3 h; (c, d) 12 h; (e, f) 20 h; (g, h) 80 h; (i, j) 104 h; (k, l) 152 h

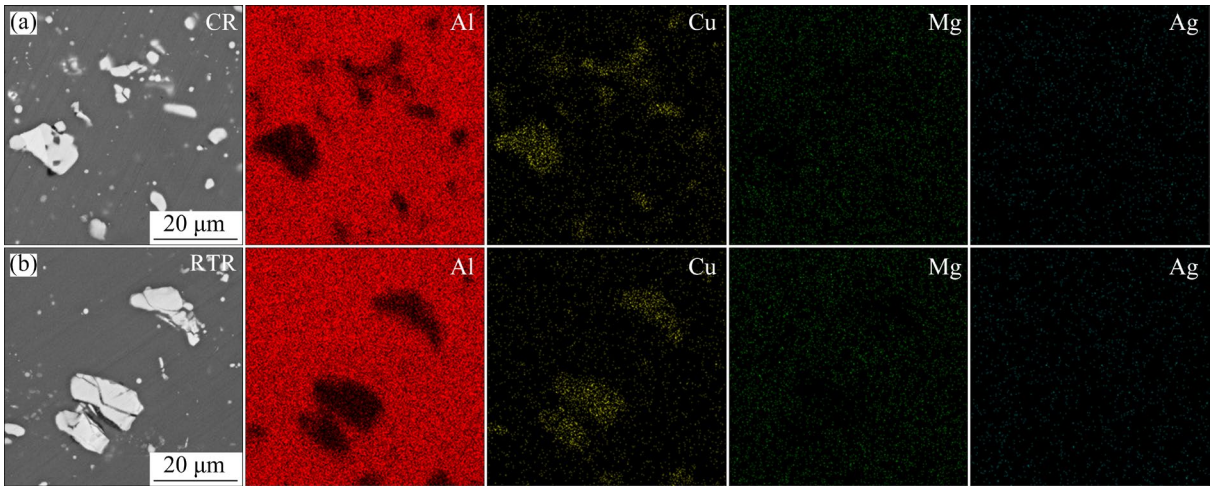

Fig. 9 SEM images and element distributions of AA2195 under different rolling conditions: (a) CR; (b) RTR

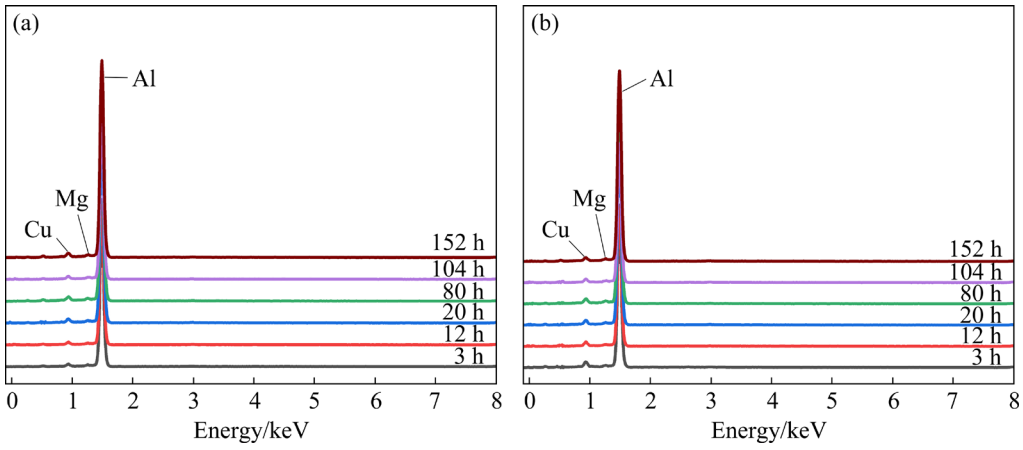

Fig. 10 EDS results of corroded surfaces of rolled and aged samples: (a) CR; (b) RTR

Figure 7 illustrates the electrochemical corrosion morphologies of the RD−TD surface of the CR sample aged at 160 °C for different durations after the potentiodynamic polarization experiment. As seen in Figs. 7(a, b), the corrosion morphology of CR samples primarily featured pitting, with only a few corrosion pits evident after aging for 3 h. With further aging for 12 h, the number of corrosion pits on the surface of the sample remained little, but the individual pit areas were large, as shown in Figs. 7(c, d). Upon reaching an aging time of 20 h, the number of corrosion pits notably increased, coupled with the emergence of slight corrosion cracking behavior at the pit edges (Figs. 7(e, f)). As apparent in Figs. 7(g, h), when the aging time was extended to 80 h, the corrosion areas increased significantly, with the corrosion crack becoming more pronounced and the proportion of the deep corrosion pit expanding. In comparison with samples aged for 80 h, the corrosion pit area of samples aged for 104 and 152 h did not undergo significant changes and still displayed a pitting morphology, characterized by larger corrosion depth at the center and corrosion cracks at the edges, as depicted in Figs. 7(i−l).

Moreover, Fig. 8 shows the electrochemical corrosion morphologies of the RD−TD surface of the RTR sample aged at 160 °C at different time after the potentiodynamic polarization experiment. After aging for 3 h, the corrosion morphology was primarily dominated by small pits. With an increase in aging time to 12 h, the number of pits increased, and the corrosion area began to grow, as depicted in Figs. 8(a−d). Subsequently, after aging for 20 h, corrosion cracks started to appear, the corrosion area increased, and areas with greater corrosion depth appeared at the center of corrosion, as displayed in Figs. 8(e, f). With the extension of aging time to 80−152 h, the density and corrosion area of the corrosion pits reached the maximum and remained relatively stable, as shown in Figs. 8(i−l).

The comparison between Figs. 7 and 8 reveal that the electrochemical corrosion morphology of CR and RTR samples consistently presented pitting morphology. The area of the corrosion pits of both samples continued to increase with the extension of aging time. However, when the aging time reached 80 h, signifying entry into the over-aging stage, the corrosion morphology of both samples no longer underwent substantial changes. The corrosion area reached its maximum and began to stabilize. The notable distinction observed was the considerably larger corrosion area of RTR samples compared to CR samples, beginning at the 12 h aging (i.e., the peak aging stage). This finding indicated a higher corrosion rate for RTR samples, reflecting inferior corrosion resistance. This was consistent with the experimental result obtained from the potentio-dynamic polarization experiment.

With closer observation of Figs. 7 and 8, it became apparent that the surface of the RD−TD sample contained numerous silver-white second phases, frequently accompanied by corrosion pits in these regions. In order to investigate the element enrichment in the second phase and corrosion pits, EDS detection was performed on the alloy surface, as illustrated in Figs. 9 and 10. The enrichment of second-phase elements on the RD−TD surface of CR and RTR samples is shown in Fig. 9. These phases are primarily enriched with elements such as Cu, with minimal presence of elements such as Al, Mg, and Ag. Throughout the corrosion process, a noticeable potential difference existed between the Cu-enriched second phase and the surrounding Al matrix. Moreover, the micro-current corrosion occurred between the second phase and the matrix, leading to the appearance of corrosion pits. The elemental content within corrosion pits on the RD−TD surface of the alloy is displayed in Fig. 10. Based on the EDS results, the distribution of elements in corrosion pits at different aging stages of both CR and RTR samples demonstrated a high degree of similarity, with the content given in Table 3.

Next, the corrosion performance of AA2195 was further verified by the EIS test. Nyquist diagrams of CR and RTR samples are respectively presented in Figs. 11(a, c). Both CR and RTR samples with varying aging times possessed similar corrosion characteristics, consisting of two parts: a high-frequency capacitive reactance region and a low-frequency inductive reactance region. To enhance the understanding of the corrosion characteristics, equivalent circuit fitting was applied to the EIS curve, with the fitting results listed in Table 4. In the equivalent circuit, R_s represents solution resistance. The constant phase angle unit CPE_1 signifies the double electric layer at the

Table 3 Element contents in corrosion pit of alloy (at.%)

Sample	Al	Cu	Mg	Ag
CR 3 h	97.28	1.75	0.63	0.34
CR 12 h	96.22	2.85	0.56	0.37
CR 20 h	97.71	1.62	0.52	0.15
CR 80 h	97.72	1.45	0.64	0.18
CR 104 h	97.61	1.75	0.48	0.16
CR 152 h	97.42	1.63	0.62	0.33
RTR 3 h	96.39	2.54	0.74	0.33
RTR 12 h	96.60	2.70	0.56	0.14
RTR 20 h	97.12	2.01	0.60	0.28
RTR 80 h	97.63	1.52	0.66	0.19
RTR 104 h	96.31	2.62	0.68	0.39
RTR 152 h	97.59	1.54	0.63	0.24

contact surface between the sample and solution. L and R_L represent the resistance and inductance of the working electrode (corroded sample), while R_{ct} is charge transfer resistance. R_s and CPE_1 constitute the high-frequency region, whereas the low-frequency region is composed of inductance L and resistance R_L. Figures 11(b, d) show Bode charts of CR and RTR samples, respectively. As the frequency decreased, the impedance modulus $|Z|$ increased, signifying superior corrosion resistance in the respective samples. Consequently, the EIS tests revealed consistent trends between CR and RTR samples, corroborating the results obtained from the potentiodynamic polarization tests.

Generally, the corrosion performance and morphology of alloys are influenced by the potential difference between the matrix and the precipitates. The type, quantity, size, and distribution of the precipitates have a substantial impact on the corrosion performance of the alloys. As observed in the preceding discussion, the corrosion morphology was changed and the electrochemical behavior of the CR and RTR samples was different.

3.3 Microstructure characterization

To study the effect of CR on the precipitates of Al−Li alloy, the grain structure of the alloy was

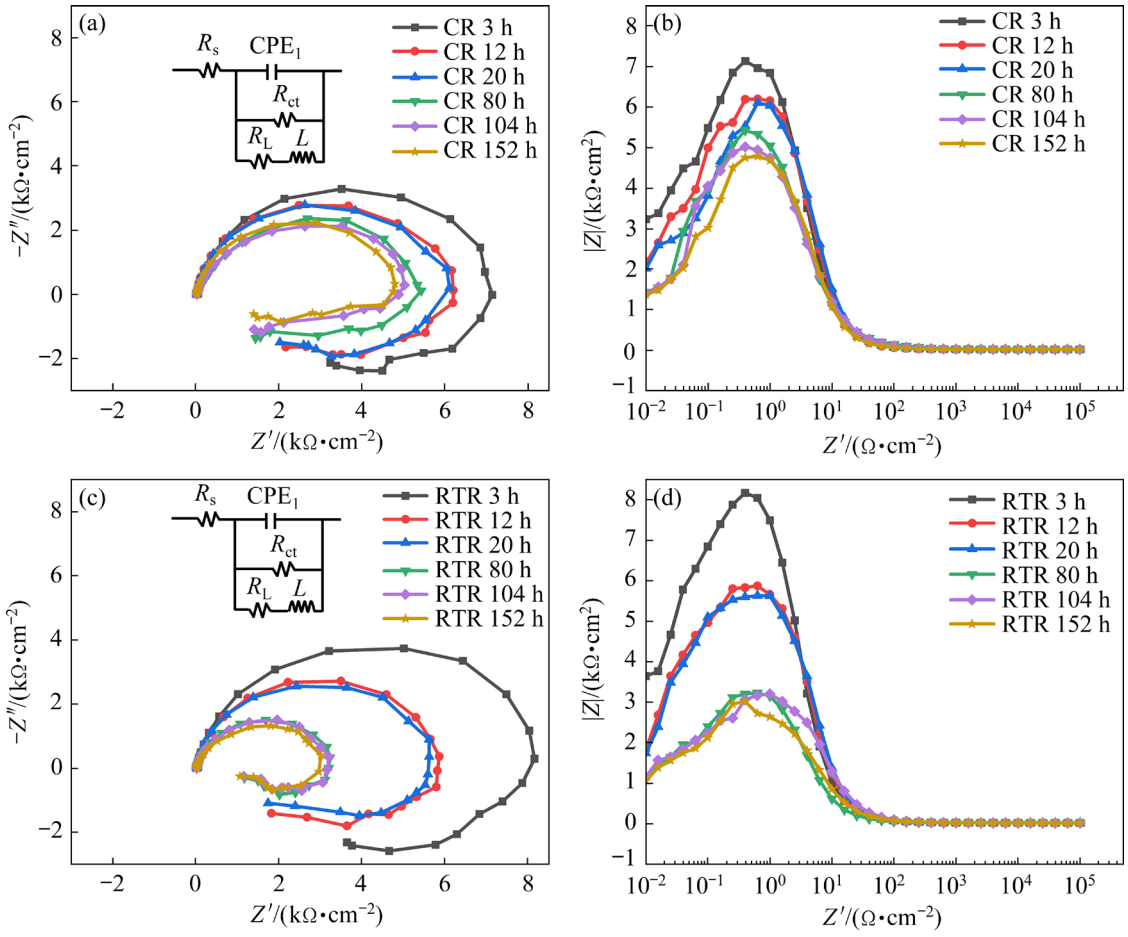

Fig. 11 Nyquist (a, c) and Bode (b, d) plots of rolled and aged samples: (a, b) CR; (c, d) RTR

Table 4 Fitting results of EIS curves

Sample	R_s/(Ω·cm^2)	CPE$_1$/(F·s^{n-1}·cm^{-2})	n_1	R_{ct}/(Ω·cm^2)	R_L/(Ω·cm^2)	L/kH
CR 3 h	17.6	1.87×10^{-5}	0.991	6849.2	3264.3	35.4
CR 12 h	18.8	1.49×10^{-5}	0.962	5728.9	2901.8	31.0
CR 20 h	18.8	1.42×10^{-5}	0.959	5564.7	2795.3	30.6
CR 80 h	20.0	1.25×10^{-5}	0.896	5491.3	2673.5	28.4
CR 104 h	19.9	1.22×10^{-5}	0.886	5287.1	2579.4	27.3
CR 152 h	21.2	1.18×10^{-5}	0.859	4508.4	2371.5	24.7
RTR 3 h	17.2	2.09×10^{-4}	0.996	8186.7	4371.9	53.8
RTR 12 h	18.8	1.37×10^{-5}	0.936	5681.5	2864.7	29.9
RTR 20 h	19.1	1.34×10^{-5}	0.936	5559.2	2830.1	28.6
RTR 80 h	20.2	1.07×10^{-5}	0.843	3831.6	2319.4	22.1
RTR 104 h	20.2	1.04×10^{-5}	0.942	3317.9	2252.7	21.3
RTR 152 h	20.9	9.62×10^{-6}	0.838	3089.8	2240.3	20.7

initially examined, with results shown in Fig. 12. Samples at different aging stages under the same rolling process displayed similar grain structures. The CR sample exhibited a finer grain size with clearly noticeable shear bands, whereas the RTR sample showed coarser grains, and the presence of shear bands was less prominent. The average grain size statistics of each sample are given in Table 5.

Due to the lack of precipitated phases in the initial aging stage, samples aged for 20 h (peak aging stage) and 80 h (over-aging stage) were selected for TEM observation along the $[110]_{Al}$ direction, as depicted in Fig. 13. After aging for 20 h, only the short T_1 phase was identified in the CR sample, with its uniform distribution (Fig. 13(a)). Notably, the T_1 phase at the grain boundary was smaller than that within the grain. In contrast, when the aging time was prolonged to 80 h, a small amount of θ' phase began to emerge in the alloy, as shown in Fig. 13(b). However, the primary T_1 precipitates remained, and over-aged T_1 phase was longer than the peak aged one. Meanwhile, for RTR samples, no other precipitates were found except for a large number of T_1 phases in 20 h aged alloy. After aging for 80 h, similar to CR samples, the T_1 phase size continued to increase, accompanied by the precipitation of a small amount of fine θ' phase. However, when comparing the CR and RTR samples, the notable distinction laid in the T_1 phase of the CR sample being shorter than that of the RTR sample with the same aging time. The statistic diagrams are shown in Fig. 14.

In addition, Fig. 14(a) illustrates the surface density of the T_1 phase of CR and RTR samples with TEM observation. More than 15 TEM images were analyzed for each alloy in different states. In each TEM image, the number of T_1 phases in the crystal was counted to estimate the surface density of T_1 precipitated phases. As shown in Fig. 14(a), the surface density of T_1 phase in both the CR and RTR samples decreased as the alloy changed from the peak aging to the over-aging stage. Notably, the surface density of T_1 phase in the CR samples decreased from 1125 to 900 μm^{-2}, while it dropped from 950 to 825 μm^{-2} in RTR samples. Specifically, the surface density of T_1 phase in the CR sample was higher than that in the RTR sample at 20 and 80 h, with a difference of 175 μm^{-2} at 20 h and 75 μm^{-2} at 80 h for CR and RTR samples, respectively. Further, Fig. 14(b) displays the size distribution of T_1 precipitated phase in TEM images. The size of T_1 phase in CR samples at 20 h was predominantly concentrated in the range of 10−30 nm, with an average size of 24 nm, representing the smallest size among all samples. The sizes of T_1 phase in CR 80 h and RTR 20 h samples were concentrated in the range of 25−45 nm, with average sizes of 36 and 39 nm, respectively. However, the size of T_1 phase in RTR 80 h samples was the largest, ranging 35−65 nm, with an average size of 49 nm.

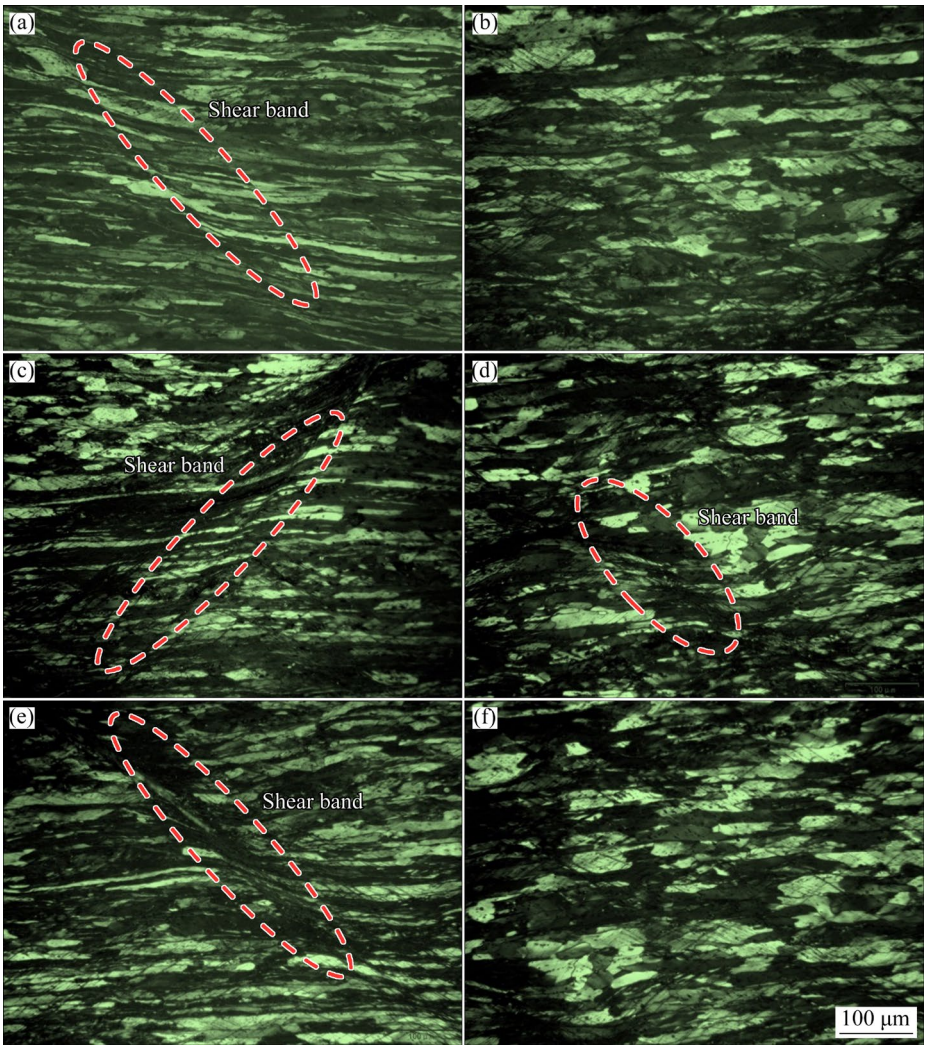

Fig. 12 Optical micrographs of microstructure of CR (a, c, e) and RTR (b, d, f) samples: (a, b) Aged for 3 h; (c, d) Aged for 20 h; (e, f) Aged for 80 h

Table 5 Average grain area of samples (μm^2)

CR 3 h	CR 20 h	CR 80 h	RTR 3 h	RTR 20 h	RTR 80 h
1055	1381	1172	1867	1974	2108

3.4 Corrosion modes of CR and RTR samples

IGC tests have revealed that aging has the potential to alter the corrosion morphology of the alloy. Similar observations were reported by JIANG et al [18] and ZHANG et al [38] indicating a comparable process wherein the corrosion mode underwent changes with aging time. During the transition from initial aging to peak aging, the corrosion morphology of the alloy shifted from uniform IGC to localized IGC. They further observed the occurrence of IGC resulting from the heterogeneous precipitation of T_1 phase, creating a potential difference between the intragranular and grain boundaries. The evolution of local IGC to IGC was attributed to the coarsening and discontinuous distribution of the precipitated phase at grain boundaries. Another contributing factor to the occurrence of IGC was the expansion of the precipitation-free zone at grain boundaries. In this study, the solid solution-treated plate underwent significant plastic deformation via either CR or RTR, followed by artificial aging treatment. In comparison with RTR, the high-temperature difference in the deformation process of CR affected the microstructure of the plate and the transformation of the corrosion mode of the alloy. Through a combination of IGC experiments, potentiodynamic polarization experiments, and TEM analysis, the mechanism of corrosion morphology transformation during the artificial aging process was demonstrated.

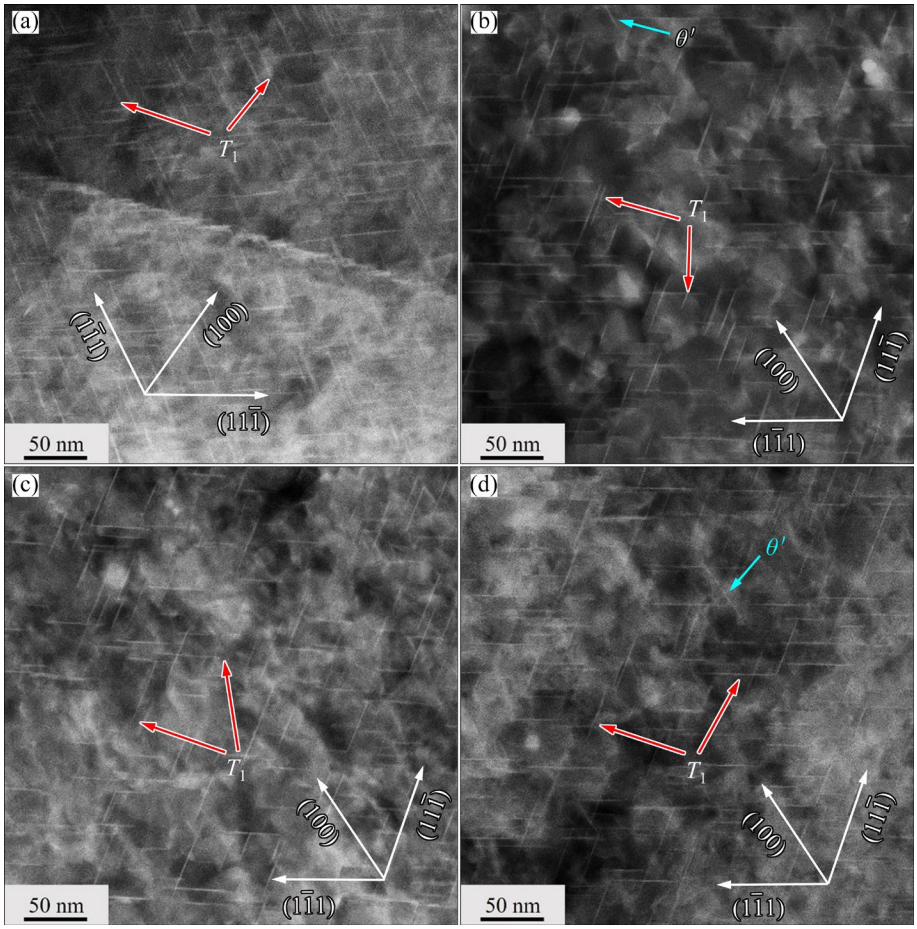

Fig. 13 $[110]_{Al}$ direction dark field micrographs of CR (a, b) and RTR (c, d) alloys aged at 160 °C for 20 h (a, c) and 80 h (b, d)

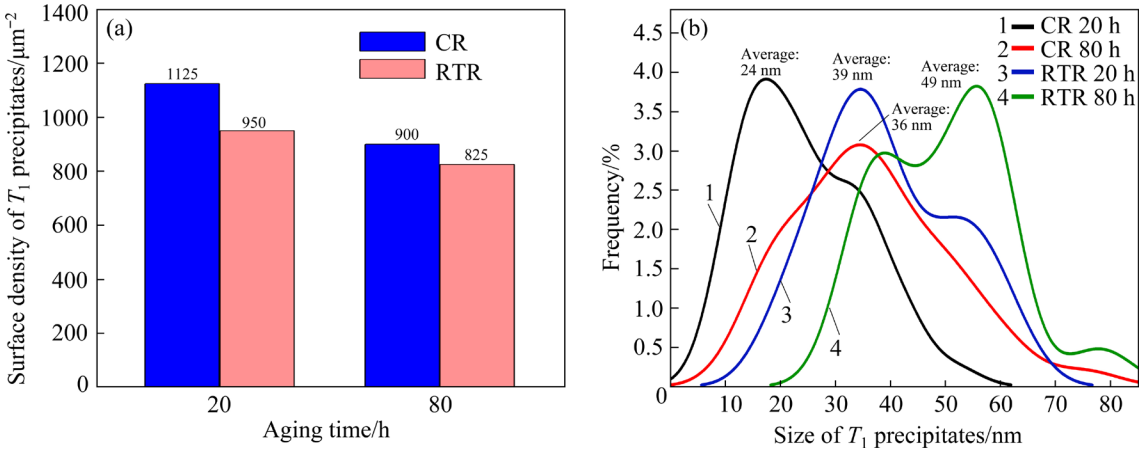

Fig. 14 Surface density (a) and size distribution (b) of T_1 precipitates in different samples measured by TEM

Moreover, the evident difference between the electrochemical behavior of the precipitated phase and the matrix underscored the significant impact their precipitation and distribution can exert on the corrosion rate of the alloy [39]. Past studies suggested that the corrosion potentials of the T_1 phase and θ' phase in a 0.6 mol/L NaCl solution were −695 mV and −1076 mV vs SCE, respectively. Compared with the Al matrix, the corrosion potentials of these three phases were as follows: T_1 phase < Al matrix < θ' phase [23,27]. However, the TEM images only revealed a small number of θ'

phases, making the T_1 phase the main focus of the analysis.

It should be mentioned that local corrosion preferably occurs in non-recrystallization regions, i.e., regions with high grain storage energy [38]. In the early stages of aging, both CR and RTR samples exhibited numerous grains with high energy storage due to severe plastic deformation. These grains contributed to the manifestation of pitting morphology in the corrosive environment. The T_1 phase demonstrated a preference for precipitation at grain boundaries and dislocations during this period [40]. During the progression of artificial aging, a large number of T_1 phases started to precipitate at dislocation and grain boundary nucleation sites, facilitated by the thermal energy generated during the artificial aging process, leading to a gradual shift into the peak aging stage. In contrast to RTR, the finer grains of CR produced more dislocations and larger grain boundary areas, thereby offering abundant nucleation sites for the precipitation of T_1 phase. Simultaneously, the inhibition of the recrystallization process by cryogenic temperature enriched the grain storage energy of CR sample [8]. The interplay of these factors promoted the precipitation of T_1 phase in Al−Li alloy. Meanwhile, accelerated precipitation of T_1 phase resulted in the CR sample reaching the peak aging stage in a shorter timeframe. The corrosion potential of T_1 phase was more negative than that of the Al matrix. In the early aging period, the substantial formation of T_1 phases at the grain boundaries led to a lower corrosion potential at the grain boundaries compared to the grain itself [22,23]. In the corrosive environment, this potential difference between the grain boundary and the grain facilitated the corrosion of the alloy, changing the corrosion morphology from the initial pitting corrosion to IGC. As the aging time extended, the continuous distribution of the T_1 phase at the grain boundary diminished, while it began to precipitate in large quantities within the grain. Further, the potential difference between the grain boundary and the grain gradually decreased until it disappeared, resulting in a pitting morphology. The schematic diagram shown in Fig. 15 illustrates the corrosion pattern evolution of the CR and RTR samples in the IGC experiment, changing from pitting to IGC and back to pitting. At the same time, the CR samples, characterized by a larger grain boundary area and higher grain storage energy, accelerated this process due to the rapid precipitation of T_1 phase. This explains why the CR samples tend to pass through the IGC stage more quickly with less detrimental impact, ultimately entering the pitting stage.

3.5 Corrosion rates of CR and RTR samples

Furthermore, the quantitative analysis of precipitates provides a more comprehensive understanding of the relationship between microstructure and the corrosion behavior of alloys. In this work, the corrosion rate of the CR and RTR samples showed a trend of initial increase followed by gradual stabilization with prolonged aging time, as reflected in the potentiodynamic polarization curve and SEM images.

In the early aging stage (3 h of aging), the corrosion current density of CR samples exceeded that of RTR samples, indicating a fast corrosion rate. This phenomenon could be attributed to two reasons, namely, the precipitated phase and non-recrystallized grain. In terms of the precipitated phase, the influence of grain refinement and the precipitation kinetics resulted in higher precipitation of T_1 phases in CR samples, lowering the corrosion potential and making them more susceptible to corrosion. For non-recrystallized grains, ZHANG et al [17] found that in 2A97-T3 Al−Li alloy, non-recrystallized grains containing several small angle grain boundaries exhibited higher corrosion sensitivity compared to those without such boundaries. The energy stored within grains (equivalent to high-density dislocation) plays a decisive role in the corrosion susceptibility of subgrain boundary in non-recrystallized grains. The higher dislocation density and grain storage in the CR sample resulted in higher corrosion density than in the RTR sample. As the alloy entered the peak aging stage (20 h of aging), signifying the end of the nucleation and growth stage of T_1 phase, the quantity gradually reached its maximum. Consequently, the corrosion current density of the CR and RTR samples increased compared to the early aging stage. Nevertheless, the RTR sample displayed an extended T_1 phase at this stage, resulting in a higher corrosion current density than the CR sample. As the alloy changed into the over-aging stage (80−152 h of aging), the T_1 phase size in both CR and RTR samples continued to grow,

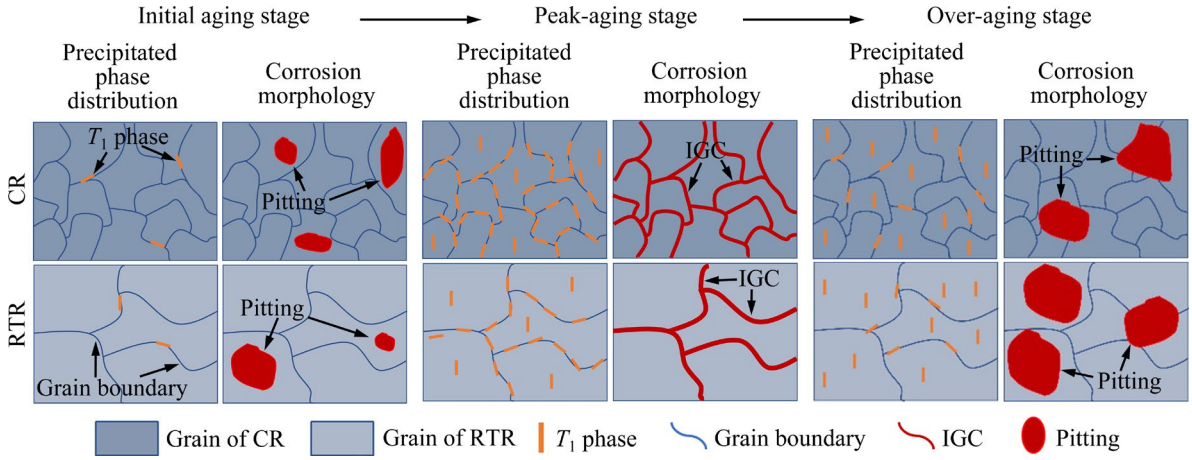

Fig. 15 Schematic diagram of corrosion morphology change principle

albeit at a lower density. Meanwhile, the corrosion current density of both samples increased and eventually stabilized. The underlying principle remained consistent with that observed in the peak aging stage, where the extended T_1 phase contributed to a higher corrosion current density in the RTR sample, leading to an elevated corrosion rate.

4 Conclusions

(1) The corrosion mode of both the CR and RTR samples during the aging treatment process followed a sequence of "pitting−IGC−pitting". Both samples exhibited an initial increase and subsequent decrease in the maximum and average corrosion depths. However, the CR sample showed a faster transformation rate in its corrosion mode, enabling it to swiftly navigate through the potentially more harmful IGC stage.

(2) At the early aging stage, the corrosion performance of the RTR sample surpassed that of the CR sample. However, upon reaching the peak aging stage and over-aging stage, the CR sample showed superior corrosion performance compared to the RTR sample.

(3) Throughout the aging process, the predominant precipitated phase in both CR and RTR AA2195 alloys was the T_1 phase, with a minor presence of the θ' phase in the over-aging stage. Notably, the CR sample displayed a higher density of precipitation compared to the RTR sample. The precipitation rate in the CR sample was larger, resulting in a longer T_1 phase in the RTR samples. Thus, the denser T_1 phase was conducive to the enhanced corrosion performance of AA2195 alloy.

CRediT authorship contribution statement

Yue XIAO: Experiments, Investigation, Writing − Original draft, Review & editing; **Wen-shuai WANG:** Investigation, Writing − Review & editing; **Waqas FARID:** Investigation, Writing – Review & editing; **Li-hua ZHANG:** Experiments, Investigation, Writing − Review & editing; **Charlie KONG:** Experiments, Investigation, Writing – Review & editing; **Hai-liang YU:** Conceptualization, Writing − Review & editing, Supervision, Project administration.

Declaration of competing interest

The authors declare that they have no known competing financial interests or personal relationships that could have appeared to influence the work reported in this paper.

Acknowledgments

This work was supported by the High-tech Industry Technology Innovation Leading Plan of Hunan Province, China (No. 2022GK4032), and the State Key Laboratory of Precision Manufacturing for Extreme Service Performance at Central South University, China.

References

[1] YU Nai-hui, SHANG Jian-zhong, CAO Yu-jun, MA Dong-xi, LIU Qi-ming. Comparative analysis of Al−Li alloy and aluminum honeycomb panel for aerospace application by structural optimization [J]. Mathematical Problems in Engineering, 2015: 815257.

[2] AHMED B, WU S. Aluminum lithium alloys (Al−Li−Cu−X)−New generation material for aerospace applications [J]. Applied Mechanics and Materials, 2014, 440: 104−111.

[3] EL-ATY A A, XU Yong, GUO Xun-zhong, ZHANG Shi-hong, MA Yan, CHEN Da-yong. Strengthening mechanisms, deformation behavior, and anisotropic mechanical properties

of Al−Li alloys: A review [J]. Journal of Advanced Research, 2018, 10: 49−67.

[4] JIANG Na, LI Jin-feng, ZHENG Zi-qiao, WEI Xiu-yu, LI Yan-fen. Effect of aging on mechanical properties and localized corrosion behaviors of Al−Cu−Li all [J]. Transactions of Nonferrous Metals Society of China, 2005, 15: 23−29.

[5] XIONG Han-qing, ZHOU Yue-xin, YANG Peng, KONG Charlie, YU Hai-liang. Effects of cryorolling, room temperature rolling and aging treatment on mechanical and corrosion properties of 7050 aluminum alloy [J]. Materials Science and Engineering A, 2022, 853: 143764.

[6] YU Hai-liang, LU Cheng, TIEU A K, LI Hui-jun, GODBOLE A, ZHANG Shi-hong. Special rolling techniques for improvement of mechanical properties of ultrafine-grained metal sheets: A review [J]. Advanced Engineering Materials, 2016, 18: 754−769.

[7] OVID'KO I A, VALIEV R Z, ZHU Y T. Review on superior strength and enhanced ductility of metallic nanomaterials [J]. Progress in Materials Science, 2018, 94: 462−540.

[8] LI Chang, XIONG Han-qing, BHATTA L, WANG Lin, ZHANG Zhao-yang, WANG Hui, KONG Charlie, YU Hai-liang. Microstructure evolution and mechanical properties of Al−3.6Cu−1Li alloy via cryorolling and aging [J]. Transactions of Nonferrous Metals Society of China, 2020, 30: 2904−2914.

[9] WU Yu-ze, ZHANG Zhao-yang, LIU Juan, KONG Charlie, WANG Yu, TANDON P, PESIN A, YU Hai-liang. Preparation of high-mechanical-property medium-entropy CrCoNi alloy by asymmetric cryorolling [J]. Transactions of Nonferrous Metals Society of China, 2022, 32: 1559−1574.

[10] LI Zhi-de, GU Hao, LUO Kai-guang, KONG Charlie, YU Hai-liang. Achieving high strength and tensile ductility in pure nickel by cryorolling with subsequent low-temperature short-time annealing [J]. Engineering, 2024, 33: 190−203. https://doi.org/ 10.1016/j.eng.2023.01.019.

[11] WANG Lin, KONG Charlie, YU Hai-liang. Mechanical property enhancement and microstructure evolution of an Al−Cu−Li alloy via rolling at different temperatures [J]. Journal of Alloys and Compounds, 2022, 900: 163442.

[12] HE Guo-ai, LI Kai, YANG Yong, LIU Yu, WU Wen-ke, HUANG Cheng. Effect of heat treatment on the microstructure and mechanical properties of cryogenic rolling 2195 Al−Cu−Li alloy [J]. Materials Science and Engineering A, 2021, 822: 141682.

[13] KUMAR V, KUMAR D. Investigation of tensile behaviour of cryorolled and room temperature rolled 6082 Al alloy [J]. Materials Science and Engineering A, 2017, 691: 211−217.

[14] WANG Lin, BHATTA L, XIONG Han-qing, LI Chang, CUI Xiao-hui, KONG Charlie, YU Hai-liang. Mechanical properties and microstructure evolution of an Al−Cu−Li alloy subjected to rolling and aging [J]. Journal of Central South University, 2021, 28: 3800−3817.

[15] LIN Y C, JIANG Yu-qiang, ZHANG Xian-cheng, DENG Jiao, CHEN Xiao-min. Effect of creep-aging processing on corrosion resistance of an Al−Zn−Mg−Cu alloy [J]. Materials & Design, 2014, 61: 228−238.

[16] LI J F, ZHENG Z Q, LI S C, CHEN W J, REN W D, ZHAO X S. Simulation study on function mechanism of some precipitates in localized corrosion of Al alloys [J]. Corrosion Science, 2007, 49: 2436−2449.

[17] ZHANG Xin-xin, ZHOU Xiao-rong, HASHIMOTO T, LIU Bing, LUO Chen, SUN Zhi-hua, TANG Zhi-hui, LU Feng, MA Yan-long. Corrosion behaviour of 2A97-T6 Al−Cu−Li alloy: The influence of non-uniform precipitation [J]. Corrosion Science, 2018, 132: 1−8.

[18] JIANG Bo, WANG Hai-sheng, TIAN Yu, YI Dan-qing, LIU Hui-qun, HU Zhan. Effects of aging time on corrosion behavior of an Al−Cu−Li alloy [J]. Corrosion Science, 2020, 173: 108759.

[19] WEN Feng, CHEN Ji-qiang, HAN Shuang, ZHOU Zi-xiang, ZHONG Shi-biao, ZHANG Ying-hui, LI Wei-rong, GUAN Ren-guo. Effect of crystal orientations and precipitates on corrosion behavior of Al−Cu−Li single crystals [J]. Transactions of Nonferrous Metals Society of China, 2022, 32: 3887−3900.

[20] XU Yue, WANG Xiao-jing, YAN Zhao-tong, LI Jia-xue. Corrosion properties of light-weight and high-strength 2195 Al−Li alloy [J]. Chinese Journal of Aeronautics, 2011, 24: 681−686.

[21] LIEW Yan-han, ÖRNEK C, PAN Jin-shan, THIERRY D, WIJESINGHE S, BLACKWOOD D J. Towards understanding micro-galvanic activities in localised corrosion of AA2099 aluminium alloy [J]. Electrochimica Acta, 2021, 392: 139005.

[22] XU X, HAO M, CHEN J, HE W, LI G, LI K, JIAO C, ZHONG X L, MOORE K L, BURNETT T L, ZHOU X. Role of constituent intermetallic phases and precipitates in initiation and propagation of intergranular corrosion of an Al−Li−Cu−Mg alloy [J]. Corrosion Science, 2022, 201: 110294.

[23] LI J F, LIAO C X, PENG Z W, CHEN W J, ZHENG Z Q. Corrosion mechanism associated with *T*1 and *T*2 precipitates of Al−Cu−Li alloys in NaCl solution [J]. Journal of Alloys and Compounds, 2008, 460: 688−693.

[24] PROTON V, ALEXIS J, ANDRIEU E, DELFOSSE J, DESCHAMPS A, GEUSER D F, LAFONT M C, BLANC C. The influence of artificial ageing on the corrosion behaviour of a 2050 aluminium–copper–lithium alloy [J]. Corrosion Science, 2014, 80: 494−502.

[25] LI J F, BIRBILIS N, LIU D Y, CHEN Y L, ZHANG X H, CAI C. Intergranular corrosion of Zn-free and Zn-microalloyed Al−*x*Cu−*y*Li alloys [J]. Corrosion Science, 2016, 105: 44−57.

[26] MA Yun-long, LI Jin-feng, ZHANG Run-zhe, TANG Jian-guo, HUANG Cheng, LI Hong-ying, ZHENG Zi-qiao. Strength and structure variation of 2195 Al−Li alloy caused by different deformation processes of hot extrusion and cold-rolling [J]. Transactions of Nonferrous Metals Society of China, 2020, 30: 835−849.

[27] BIRBILIS N, BUCHHEIT R G. Electrochemical characteristics of intermetallic phases in aluminum alloys: An experimental survey and discussion [J]. Journal of the Electrochemical Society, 2005, 152(4): 140−151.

[28] DUAN Shu-wei, GUO Fu-qiang, WU Dong-ting, WANG Tao, TSUCHIYA T, MATSUDA K, ZOU Yong. Influences of pre-rolling deformation on aging precipitates and mechanical properties for a novel Al−Cu−Li alloy [J]. Journal of Materials Research and Technology, 2021, 15: 2379−2392.

[29] LIU Dan-yang, MA Yun-long, LI Jin-feng, ZHANG Rui-feng, IWAOKA H, HIROSAWA S. Precipitate microstructures, mechanical properties and corrosion resistance of Al−1.0wt.%Cu−2.5wt.%Li alloys with different micro-alloyed elements addition [J]. Materials Characterization, 2020, 167: 110528.

[30] LIN Yi, LU Chan-ge, WEI Cheng-yang, ZHENG Zi-qiao. Effect of aging treatment on microstructures, tensile properties and intergranular corrosion behavior of Al−Cu−Li

alloy [J]. Materials Characterization, 2018, 141: 163−168.
[31] VIGNESHWARAN S, SIVAPRASAD K, NARAYANA-SAMY R, VENKATESWARLU K. Microstructure and mechanical properties of Al−3Mg− 0.25Sc alloy sheets produced by cryorolling [J]. Materials Science and Engineering A, 2019, 740/741: 49−62.
[32] AYDIN F. A review of recent developments in the corrosion performance of aluminium matrix composites [J]. Journal of Alloys and Compounds, 2023, 949: 169508.
[33] LYNCH S. A review of underlying reasons for intergranular cracking for a variety of failure modes and materials and examples of case histories [J]. Engineering Failure Analysis, 2019, 100: 329−350.
[34] FAN Le-tian, MA Ji-jun, ZOU Cheng-xiong, GAO Jun, WANG Hai-sheng, SUN Jing, GUAN Quan-mei, WANG Jun, TANG Bin, LI Jin-shan, WANG W Y. Revealing foundations of the intergranular corrosion of 5XXX and 6XXX Al alloys [J]. Materials Letters, 2020, 271: 127767.
[35] HUANG Jia-lei, LI Jin-feng, LIU Dan-yang, ZHANG Rui-feng, CHEN Yong-lai, ZHANG Xu-hu, MA Peng-cheng, GUPTA R K, BIRBILIS N. Correlation of intergranular corrosion behaviour with microstructure in Al−Cu−Li alloy [J]. Corrosion Science, 2018, 139: 215−226.
[36] CHEN Jun-feng, ZHANG Xing-feng, ZOU Lin-chi, YU Yan, LI Qiang. Effect of precipitate state on the stress corrosion behavior of 7050 aluminum alloy [J]. Materials Characterization, 2016, 114: 1−8.
[37] AJAY KRISHNAN M, RAJA V S, SHUKLA S, VAIDYA S M. Mitigating intergranular stress corrosion cracking in age-hardenable Al−Zn−Mg−Cu alloys [J]. Metallurgical and Materials Transactions A, 2018, 49: 2487−2498.
[38] ZHANG Xin-xin, LV You, ZHOU Xiao-rong, HASHIMOTO T, MA Yan-long. Corrosion behaviour of 2A97-T8 Al−Cu−Li alloy extrusion [J]. Journal of Alloys and Compounds, 2022, 898: 162872.
[39] LI H Y, KANG W, LU X C. Effect of age-forming on microstructure, mechanical and corrosion properties of a novel Al−Li alloy [J]. Journal of Alloys and Compounds, 2015, 640: 210−218.
[40] WANG Xi, RONG Qi, SHI Zhu-sheng, LI Yong, CAO Jun-xia, CHEN Bao-guo, LIN Jian-guo. Investigation of stress effect on creep, precipitation and dislocation evolution of Al−Li alloy during creep age forming [J]. Materials Science and Engineering A, 2022, 836: 142723.

深冷轧制与时效处理提升 2195 铝锂合金腐蚀性能的机理

肖 岳[1,2]，王文帅[1,2]，Waqas FARID[1,2]，张立华[1,2]，Charlie KONG[3]，喻海良[1,2]

1. 中南大学 极端服役性能精准制造全国重点实验室，长沙 410083；
2. 中南大学 轻合金研究所，长沙 410083；
3. Mark Wainwright Analytical Centre, University of New South Wales, Sydney, NSW 2052, Australia

摘 要：通过透射电子显微镜、扫描电子显微镜、光学显微镜、晶间腐蚀实验和电化学实验等研究了深冷轧制、室温轧制及其后续人工时效对 2195 铝锂合金腐蚀性能的影响。在时效处理的不同阶段，深冷轧制和室温轧制 2195 铝锂合金均呈现“点蚀−晶间腐蚀−点蚀”的腐蚀模式，二者的腐蚀速率均呈现先增大后逐渐稳定的趋势。T_1 相的尺寸与密度对合金的腐蚀性能产生重要影响，在峰时效与过时效阶段，更细小的 T_1 相使得深冷轧制样品的耐腐蚀性能更优。

关键词：2195 铝锂合金；深冷轧制；时效处理；腐蚀性能

(Edited by Bing YANG)